


Possible quadrupole-order-driven commensurate-incommensurate phase transition in B20 CoGeS.-H. Baek^{1,2,*}, V. A. Sidorov³, A. V. Nikolaev⁴, T. Klimczuk^{5,6}, F. Ronning⁷ and A. V. Tsvyashchenko³¹*Department of Physics, Changwon National University, Changwon 51139, Korea*²*Department of Materials Convergence and System Engineering, Changwon National University, Changwon 51139, Korea*³*Vereshchagin Institute for High Pressure Physics, RAS, 108840 Moscow, Troitsk, Russia*⁴*Skobel'syn Institute of Nuclear Physics, Lomonosov Moscow State University, 119991 Moscow, Russia*⁵*Faculty of Applied Physics and Mathematics, Gdansk University of Technology, Narutowicza 11/12, 80-233 Gdansk, Poland*⁶*Advanced Materials Centre, Gdansk University of Technology, Narutowicza 11/12, 80-233 Gdansk, Poland*⁷*Los Alamos National Laboratory, MPA-CMMS, Los Alamos, New Mexico 87545, USA* (Received 14 December 2021; revised 15 February 2022; accepted 6 April 2022; published 18 April 2022)

The B20-type cobalt germanide CoGe was investigated by measuring the specific heat, resistivity, and ⁵⁹Co nuclear magnetic resonance (NMR). We observed a phase transition at $T_Q = 13.7$ K, evidenced by a very narrow peak of the specific heat and sharp changes of the nuclear spin-spin (T_2^{-1}) and spin-lattice (T_1^{-1}) relaxation rates. The fact that the entropy release is extremely small and the Knight shift is almost independent of temperature down to low temperatures as anticipated in a paramagnetic metal indicates that the T_Q transition is of nonmagnetic origin. In addition, we detected a crossover scale $T_0 \sim 30$ K below which the resistivity and the NMR linewidth increase, and T_1^{-1} is progressively distributed in space, that is, a static and dynamical spatial inhomogeneity develops. While the order parameter for the T_Q transition remains an open question, a group-theoretical analysis suggests that the finite electric quadrupole density arising from the low local site symmetry at cobalt sites could drive the crystal symmetry lowering from the $P2_13$ symmetry that is commensurate to the $R3$ symmetry with an incommensurate wave vector, which fairly well accounts for the T_Q transition. The quadrupole-order-driven commensurate-incommensurate phase transition may be another remarkable phenomenon arising from the structural chirality inherent in the noncentrosymmetric B20 family.

DOI: [10.1103/PhysRevB.105.165132](https://doi.org/10.1103/PhysRevB.105.165132)**I. INTRODUCTION**

Transition-metal monosilicides MSi and -germanides MGe with the B20 cubic structure, where M denotes a transition metal such as Mn, Fe, and Co, are noncentrosymmetric materials carrying inherent structural chirality (lack of mirror symmetry) which has a drastic influence on the electronic and magnetic properties of these materials, being of recent special interest from both fundamental and technical points of view [1]. On one hand, the structural chirality causes finite spin-orbit-driven Dzyaloshinskii-Moriya interaction, which competes with the Heisenberg exchange coupling. As a result, a helical spin ordered state whose chirality is determined by the structural one [2] is stabilized as observed in MnSi [3,4], FeGe [5], MnGe [6–8], and $Fe_{1-x}Co_xSi$ [9]. It has been shown that the application of a small magnetic field in these materials generates peculiar particlelike localized spin textures, such as magnetic skyrmion lattices in MnSi [10,11] and $Fe_{1-x}Co_xSi$ [12,13], a topological spin texture in MnGe [14], and chiral magnetic bobbars in FeGe [15]. Furthermore, under hydrostatic pressure, chiral magnets undergo a quantum phase transition into a non-Fermi liquid for MnSi [16,17] or an inhomogeneous chiral-spin state for FeGe [18]. On the other hand, for nonmagnetic systems, e.g., CoSi and RhSi, the structural chirality results in a three-dimensional chi-

ral topological semimetal featured by unconventional chiral fermions [19–24] and a circular photogalvanic effect [25,26]. Interestingly, chiral magnetism with skyrmionic spin texture could be achieved in $Co_{1+x}Si_{1-x}$ alloys for $x \geq 0.028$ [27].

While the structural chirality is an essential feature of the B20 binary compounds, the electron count in the $3d$ electron shell of the transition element M is another crucial factor for the ground state. On the other hand, the structural chirality should have a considerable effect on an unfilled $3d$ shell of M , regardless of the detailed valence state which is not well defined in the B20 alloys (for example, see [29]). That is, since the local site symmetry at M is quite low in the B20 structure, the partial occupation of the $3d$ shell implies that the density matrix elements $\langle \psi_{lm} | \rho_{L,M} | \psi_{l'm} \rangle$ ($l = l' = 2$ for d functions) have a significant quadrupole electron density at corresponding crystal sites. The quadrupole contributions could arise also from the mixture of $3d$ and $4s$ functions, $\langle \psi_{lm} | \rho_{L,M} | \psi_{l'=0} \rangle$, where the function $\psi_{l'=0}$ refers to the $4s$ states [30]. The appreciable quadrupole density can lead to strong anisotropic electronic interactions which can drive a structural or quadrupole phase transition [30–32]. Such a situation is not uncommon for $4f$ and $5f$ elements, where a quadrupole moment is caused by mixing of f states [31,32], as observed in, for example, CeB_6 ($T_Q = 3.3$ K) [31,33], $TmTe$ ($T_Q = 1.8$ K) [34], and NpO_2 ($T_Q = 25.5$ K) [31]. Quadrupole phase transitions are, however, quite rare in $3d$ based compounds.

*sbaek.fu@gmail.com

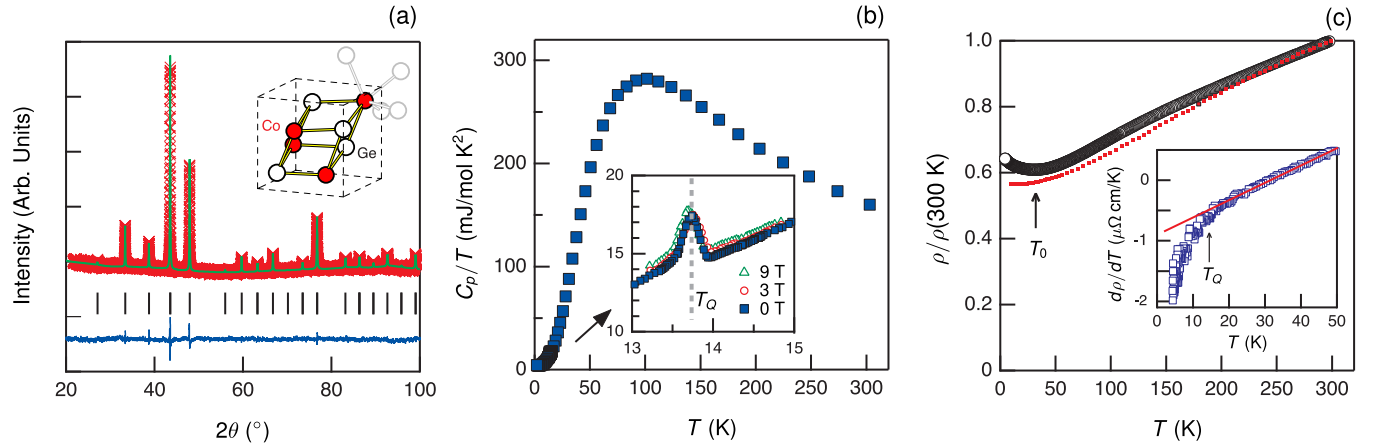


FIG. 1. (a) X-ray powder diffraction pattern of CoGe measured at $T = 295$ K at ambient pressure. The experimental points (red marks), the calculated profile (green line), and their difference (blue line) are shown. The black bars in the lower part of the graph represent the calculated Bragg reflections that correspond to the B20 structure. (b) The specific heat divided by temperature of CoGe between 2 K and 300 K. The inset enlarges the data near the sharp peak found at $T_Q = 13.7$ K. The peak is almost robust against the magnetic field up to 9 T. (c) Temperature dependence of the resistivity of CoGe, normalized at 300 K, which forms a minimum at $T_0 \sim 30$ K. The dotted data were taken from DiTusa *et al.* [28]. The inset shows $d\rho(T)/dT$ versus T at low temperatures.

In this paper, we carried out an experimental and theoretical investigation in B20 CoGe, one of the least studied B20 compounds partly due to the difficulty in synthesizing B20-type CoGe which requires the application of high pressure and temperature [35,36]. So far, B20 CoGe has been known as a Pauli paramagnet with a low carrier density without a phase transition [28,37,38], similar to the silicide counterpart CoSi, while being distinguished from other close germanides FeGe and MnGe that are helimagnets. In fact, the band crossings in the Γ and R points of the Brillouin zone in CoGe [28,38] bear remarkable resemblance to those in CoSi [22], suggesting that CoGe could host unconventional chiral fermions.

While as yet little was known of a phase transition other than the magnetic one in the B20 family, our experimental findings, such as anomalous changes of the ^{59}Co nuclear relaxation rates and a very sharp peak in the specific heat, evidence the occurrence of a nonmagnetic phase transition at $T_Q = 13.7$ K in CoGe. By performing a group-theoretical analysis, we propose that the T_Q phase transition may be a commensurate-incommensurate structural transition driven by electric quadrupole density which arises from the structural chirality. Our experimental data further suggest that some spatial inhomogeneity develops at a higher temperature $T_0 \sim 30$ K than T_Q .

II. EXPERIMENTAL DETAILS

Polycrystalline samples of B20-cubic CoGe were synthesized under a pressure of 8 GPa and at high temperatures of 1500–1700 K using a toroidal high pressure apparatus [39] by melting Co and Ge [40]. The purity was 99.9% for Co and 99.999% for Ge. The B20 phase of high pressure synthesized samples remains metastable after the pressure release at room temperature, while the monoclinic phase appears only after heating the sample above 1000 K at ambient pressure. The crystal structure was examined by x-ray diffraction (XRD), as shown in Fig. 1(a). Measurements were performed at room temperature and ambient pressure using the diffractometer

STOE IPDS-II (Mo $K\alpha$) and Guinier camera e G670, Huber (Cu $K\alpha$ 1). Powder x-ray diffraction revealed a single phase material with cubic B20-type structure. The lattice parameter of CoGe (0.46392 nm) is close to those published earlier (0.4637 nm [35] and 0.4631 nm [36] for CoGe). In the B20 structure both Co and Ge are located at the Wyckoff positions ($4a$) with coordinates (u, u, u) , $(u + 0.5, 0.5 - u, -u)$, $(-u, 0.5 + u, 0.5 - u)$, and $(0.5 - u, -u, 0.5 + u)$. Our refinement determined u to be 0.133 for Co and 0.838 for Ge. Also, the Rietveld fit of the x-ray powder diffractogram shows that the site population ratio Co/Ge is 0.999(5), evidencing a negligibly small intermixing between the two ions.

Measurements of the specific heat C_p were performed using the Quantum Design Physical Properties Measurement System (PPMS). Resistivity ρ was measured by a four-terminal method using spot welded Pt wires as the electrodes.

^{59}Co (nuclear spin $I = 7/2$) NMR experiments were carried out at the external magnetic field of $H = 3$ T in the temperature range $T = 2.5$ –200 K. The NMR spectra and the spin-spin relaxation rate T_2^{-1} were obtained using the Hahn echo sequence with a typical $\pi/2$ pulse length of ~ 3 μs . For the full spectra including satellite transitions, we used a frequency-sweep method. The spin-lattice relaxation rate T_1^{-1} was measured by the saturation method on the first satellite line and determined by fitting the recovery curve of the nuclear magnetization $M(t)$ to the appropriate fitting function for the first satellite transition in the $I = 7/2$ case with the inclusion of a stretching exponent β , i.e.,

$$1 - \frac{M(t)}{M(\infty)} = A \left[\frac{1}{84} e^{-(t/T_1)^\beta} + \frac{1}{84} e^{-(3t/T_1)^\beta} + \frac{1}{33} e^{-(6t/T_1)^\beta} + \frac{9}{77} e^{-(10t/T_1)^\beta} + \frac{1}{1092} e^{-(15t/T_1)^\beta} + \frac{49}{132} e^{-(21t/T_1)^\beta} + \frac{196}{429} e^{-(28t/T_1)^\beta} \right], \quad (1)$$

where A is a fitting parameter that is ideally one.

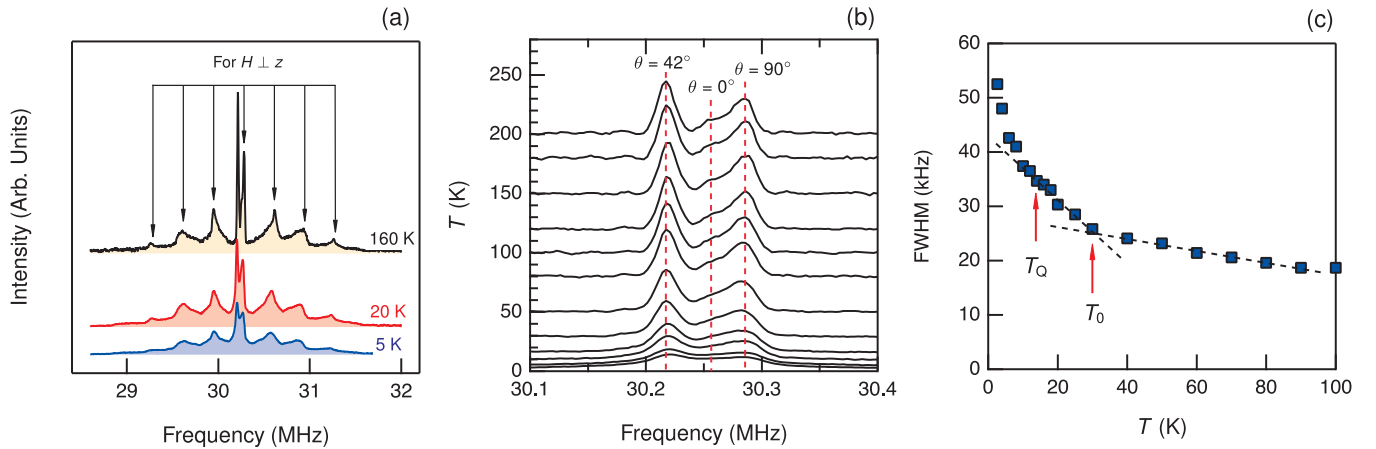


FIG. 2. (a) ^{59}Co NMR spectra obtained at 3 T by a frequency sweep. They show a typical spectral pattern found in a randomly oriented powder for $I = 7/2$ nuclei with near axial symmetry. The vertical arrows are expected lines for $H \perp z$ ($\theta = 90^\circ$) in the absence of asymmetry ($\eta = 0$). With lowering temperature, the spectrum is moderately broadened with a small reduction of the separation of satellites. (b) The spectrum at the central transition which is determined by the second order quadrupole shift as a function of temperature. The two maxima as well as the $\theta = 0^\circ$ position are nearly unshifted with lowering temperature, indicating that the Knight shift is unchanged. (c) Temperature dependence of the FWHM of the lower central peak in (b). Anomalous increase of the FWHM at $T_0 \sim 30$ K is noticed. The dotted lines are a guide to the eyes to emphasize the anomaly at T_0 .

III. RESULTS

A. Specific heat and resistivity

The specific heat divided by temperature, C_p/T , as a function of temperature is shown in Fig. 1(b). While the data are consistent with the previous results reported in the literature [28,37], we detected a weak but very sharp peak at $T_Q = 13.7$ K, as shown in the inset of Fig. 1(b), which has been overlooked so far. There are two important features of this specific heat peak that are prominent: (i) the peak position and amplitude are nearly independent of external magnetic field strength up to 9 T and (ii) an extremely small magnetic entropy is released around the transition [$\Delta S = 0.89$ mJ/mol K = $0.00015(R \ln 2)$]. Because the uniform magnetic susceptibility $\chi(T)$ does not exhibit any anomaly near T_Q [37], these features indicate that the transition is of nonmagnetic origin. Below, we will show that the low energy spin/charge dynamics probed by the ^{59}Co relaxation rates exhibit clear anomalous changes at T_Q , while the Knight shift, or the local static spin susceptibility, is unchanged through T_Q , demonstrating that the T_Q transition is an intrinsic bulk property of the material.

Resistivity measurements were performed on a few samples synthesized at high pressure. General behavior of $\rho(T)$ for all samples is similar, while they differ in the value of the residual resistivity. Representative $\rho(T)/\rho(300$ K) data of CoGe are shown in Fig. 1(c). We also compared the data from DiTusa *et al.* [28]. Metallic behavior in $\rho(T)$ is observed at high temperatures between 30 and 300 K. However, our $\rho(T)$ data reveal a distinguished feature at low temperatures: $\rho(T)$ passes through a minimum at a characteristic temperature $T_0 \sim 30$ K and is slightly enhanced upon further cooling. It appears that $\rho(T)$ is quite symmetric around T_0 , as evidenced by the linear temperature derivative of the resistivity, $d\rho(T)/dT$, between T_Q and 50 K [see red line in the inset of Fig. 1(c)]. The enhancement of $\rho(T)$ at low temperatures resembles the

Kondo effect, but it should be noted that the γ value estimated from the C/T data is only about 3 mJ/mol K², which is comparable to the free electron value. Also, there is no signature of magnetic screening from the susceptibility measurements [28,37]. Therefore, the enhanced resistivity below T_0 may be related with a spatial inhomogeneity as discussed below.

B. ^{59}Co NMR spectrum and Knight shift

Figure 2(a) shows the quadrupole-perturbed ^{59}Co spectra in CoGe obtained by a frequency sweep method at 3 T at three selected temperatures. For a nuclear spin $I > 1/2$ in an axial symmetric surrounding (asymmetry parameter $\eta = 0$), to first order, there are central ($-\frac{1}{2} \leftrightarrow \frac{1}{2}$) and satellite transitions between the m th and $(m-1)$ th levels ($m = -I, -I+1, \dots, +I$) which are given by

$$\nu(m \leftrightarrow m-1) = \nu_0(1 + \mathcal{K}) + \frac{1}{2}\nu_Q(3 \cos^2 \theta - 1)(m - \frac{1}{2}), \quad (2)$$

where \mathcal{K} is the Knight shift, ν_0 is the unshifted Larmor frequency, ν_Q is the nuclear quadrupole frequency, and θ is the angle between the principal axis z of the electric field gradient (EFG), which is most likely along the diagonals, and an external field H .

The observed full NMR spectrum is roughly described by Eq. (2) in a randomly oriented powder, in which the $m \leftrightarrow m-1$ transitions for $\theta = 90^\circ$ ($H \perp z$) form the sharp satellite peaks which are equally spaced by $\nu_Q/2$, indicating that the local symmetry at ^{59}Co is close to axial. Nevertheless, we find that the positions of two outer pairs of satellites slightly differ from the expected ones for $\eta = 0$, implying a finite asymmetry. In this case, the distance between the first satellites is equivalent to the *apparent* quadrupole frequency ν'_Q that is related to the actual value by $\nu_Q = \nu'_Q/(1 - \eta)$ [41].

In addition to the first order quadrupole effect, there is also a second order quadrupole effect which shifts the central transition ($-\frac{1}{2} \leftrightarrow \frac{1}{2}$) depending on θ . For $I = 7/2$, it is written

$$\nu\left(-\frac{1}{2} \leftrightarrow \frac{1}{2}\right) = \nu_0(1 + \mathcal{K}) + \frac{15\nu_Q^2}{16\nu_0}(1 - \cos^2\theta)(1 - 9\cos^2\theta). \quad (3)$$

The powder pattern of the central transition as a function of temperature is presented in Fig. 2(b). It reveals two peaks which correspond to the lines for $\theta \sim 42^\circ$ and 90° at which the second order quadrupole shift is minimal and maximal, respectively, as can be easily verified in Eq. (3). The separation between the two maxima $\Delta\nu$ depends on η as well as ν_Q [41]:

$$\Delta\nu = \frac{15\nu_Q^2}{144\nu_0}(\eta^2 + 22\eta + 25), \quad (4)$$

where $\nu_Q = \nu'_Q/(1 - \eta)$. Since $\Delta\nu$ is only slightly decreased at low temperatures without a noticeable anomaly, we compare the ν_Q and η values at the two temperatures, 160 K and 5 K, at which the full spectra are available. By using the ν'_Q values extracted from the full spectra in Fig. 2(a), Eq. (4) yields $\eta = 0.191$ at 160 K and $\eta = 0.222$ at 5 K which, in turn, give rise to $\nu_Q = 0.821$ MHz at 160 K and 0.793 MHz at 5 K. This shows that the asymmetry is indeed finite reflecting the low local site symmetry at ^{59}Co with weak temperature dependence.

Unlike the two sharp maxima for the central transition, the $\theta = 0^\circ$ line, which often appears as a steplike anomaly in a clean sample as observed at high temperatures [see the dotted line for $\theta = 0^\circ$ in Fig. 2(b)], is unaffected by quadrupole effects up to second order, and thus permits us to deduce the Knight shift \mathcal{K} . Although the steplike anomaly gradually smears out at low temperatures due to line broadening, the data indicate that the Knight shift is essentially independent of temperature down to 2.5 K, evidencing that the system remains a Pauli paramagnet regardless of the T_Q phase transition.

Another interesting feature found in Figs. 2(a) and 2(b) is the broadening of the NMR spectrum at low temperatures. As shown in Fig. 2(c), the full width at half maximum (FWHM) measured on the left central peak for $\theta = 42^\circ$ is more rapidly enhanced below $T_0 \sim 30$ K, suggesting that a static spatial inhomogeneity develops below T_0 and becomes even stronger at low temperatures toward zero temperature.

C. ^{59}Co nuclear relaxation rates

Figure 3(a) shows the decay of the nuclear magnetization M_n of ^{59}Co at three selected temperatures, being normalized at zero time. M_n is described by both the Lorentzian and Gaussian spin-spin relaxation rate, T_{2L}^{-1} and T_{2G}^{-1} :

$$M_n(2\tau) = M_0 \exp\left(-\frac{2\tau}{T_{2L}}\right) \exp\left[-\frac{1}{2}\left(\frac{2\tau}{T_{2G}}\right)^2\right], \quad (5)$$

where τ is the delay time between the echo pulses. In general, the two rates result from different relaxation processes: while

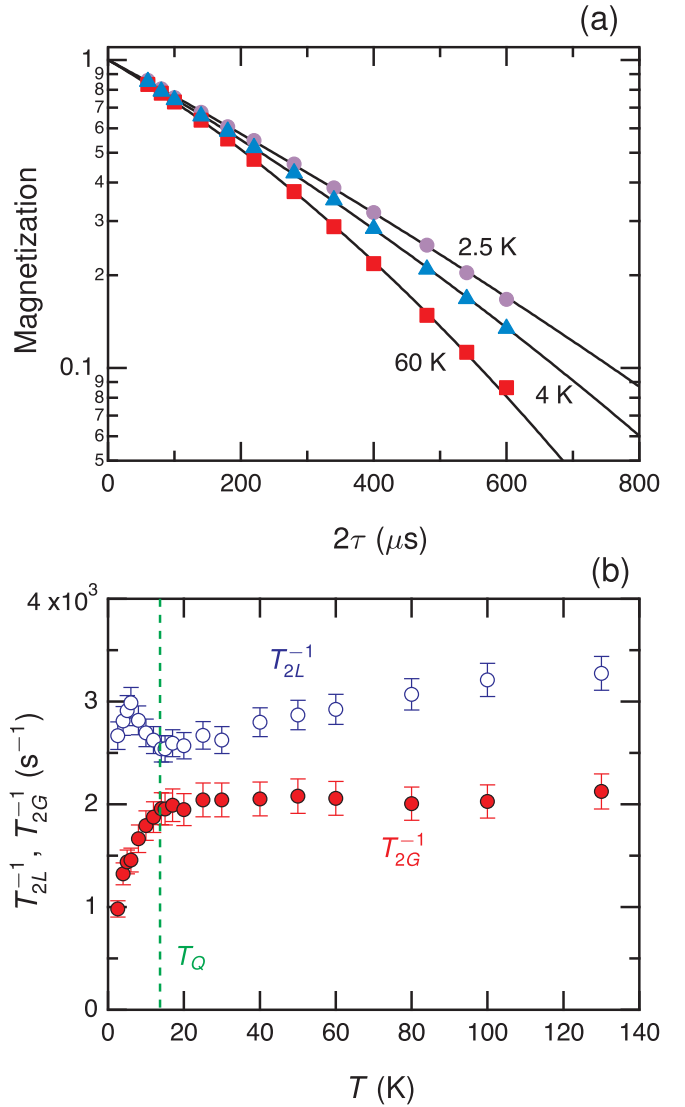


FIG. 3. (a) Decay of the nuclear magnetization M_n of ^{59}Co with time 2τ at selected temperatures. At low temperatures, the Lorentzian rate T_{2L}^{-1} becomes dominant over the Gaussian one T_{2G}^{-1} . (b) Temperature dependence of T_{2L}^{-1} and T_{2G}^{-1} . The sharp anomalous changes of both rates are observed at $T_Q = 13.7$ K.

T_{2L}^{-1} is the contribution from the spin-lattice relaxation process, T_{2G}^{-1} describes the indirect coupling between neighboring nuclear spins through electronic excitations [42]. Clearly, as shown in Fig. 2(b), both T_{2L}^{-1} and T_{2G}^{-1} significantly change at $T_Q = 13.7$ K. Below T_Q , T_{2L}^{-1} is enhanced forming a peak centered at ~ 7 K. One can see that its temperature dependence is quite similar to that of T_1^{-1} [see Fig. 4(a)], supporting the direct relationship between T_{2L}^{-1} and T_1^{-1} . In contrast, the Gaussian contribution T_{2G}^{-1} is nearly temperature independent at high temperatures, but rapidly decreases with decreasing temperature below T_Q , contrasting sharply with the upturn of T_{2L}^{-1} .

The measurement of the spin-lattice relaxation rate T_1^{-1} was carried out in the relatively low temperature region $T \leq 60$ K. The results are shown in Fig. 4(a). T_1^{-1} is proportional to T down to 30 K, or the constant $(T_1 T)^{-1}$, as shown in

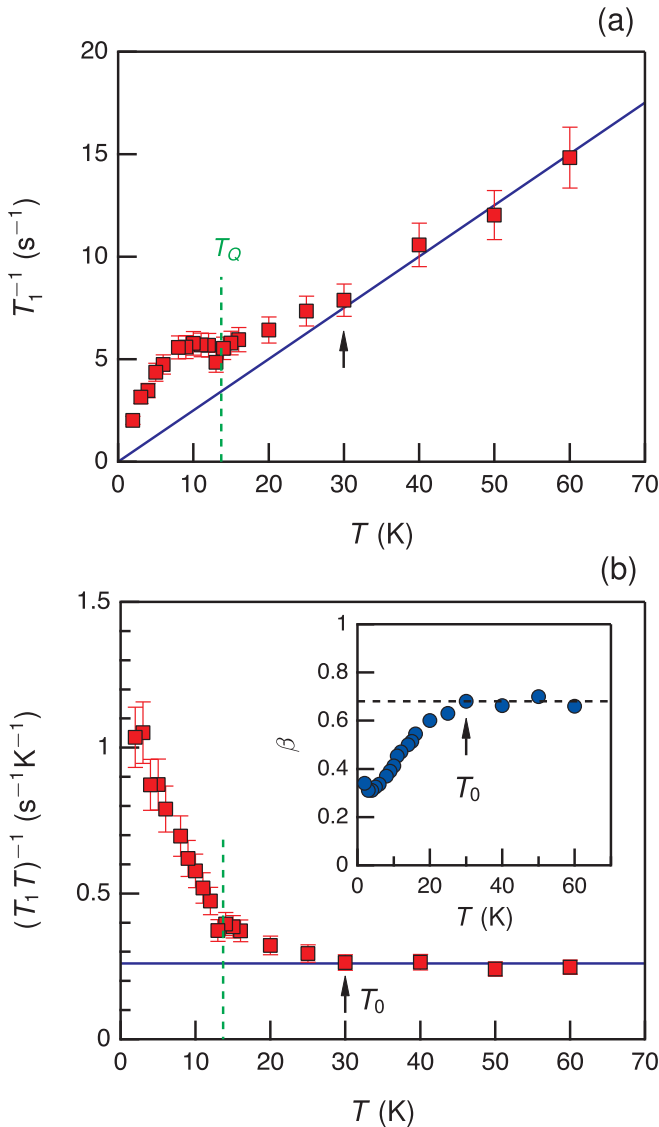


FIG. 4. Temperature dependence of (a) T_1^{-1} and (b) $(T_1T)^{-1}$. The data deviate from the linear T dependence roughly below $T_0 \sim 30$ K and reveal a small kink at $T_Q = 13.7$ K followed by a rapid increase of $(T_1T)^{-1}$. The inset shows the temperature dependence of the stretching exponent β , which is a measure of a dynamical spatial inhomogeneity.

Fig. 4(b). Together with the T -independent Knight shift, this indicates that the so-called Korringa law $(T_1T)\mathcal{K}^2 = \text{const}$, which is expected in a normal metal, holds. Below $T_0 \sim 30$ K, however, the Korringa behavior breaks down. At the same time, we find that the stretching exponent β [see Eq. (1)], shown in the inset of Fig. 4(b), decreases from a constant below T_0 , indicating that T_1^{-1} is progressively distributed in space. Remarkably, the temperature at which β begins to decrease is very close to T_0 at which the resistivity $\rho(T)$ forms a minimum [see Fig. 1(c)] and the NMR linewidth increases more rapidly [see Fig. 2(c)]. These findings strongly suggest that $T_0 \sim 30$ K indeed represents a crossover scale below which a both *static and dynamical* spatial inhomogeneity of electronic phases begins to develop. Also, we note that β is a constant but still notably smaller than unity above T_0 ,

suggesting that a temperature-independent weak spatial inhomogeneity already exists at high temperatures.

Upon further cooling, we find an additional increase of $(T_1T)^{-1}$ just below T_Q . Since the system remains a paramagnetic metal down to very low temperatures, the increase of $(T_1T)^{-1}$ below T_Q suggests that the T_Q transition is intimately related to a slowing of collective spin/charge fluctuations. Regardless of the underlying mechanism, the clear changes of the nuclear relaxation rates, T_{2L}^{-1} , T_{2G}^{-1} , and $(T_1T)^{-1}$, at T_Q demonstrate that the T_Q transition is the intrinsic bulk property of B20 CoGe.

IV. DISCUSSION

Combining our experimental findings, it is clear that a spatially inhomogeneous phase appears below a crossover scale $T_0 \sim 30$ K and a nonmagnetic long-range phase transition occurs at $T_Q = 13.7$ K in B20 CoGe. In order to obtain further insights into the possible order parameter for the T_Q transition and the underlying origin of the spatial inhomogeneity developed below T_0 , we employ group theory methods as follows.

As the B20 structure with the $P2_13$ space group symmetry ($\Gamma_c T^4$, no. 198) lacks inversion symmetry, the local site symmetry in CoGe is quite complicated. There are four different threefold rotational axes directed along the cube diagonals, but they intersect at different cobalt and germanium atoms. This symmetry imposes a certain restriction on the electron density component expressed in terms of spherical harmonics Y_L^M about atoms. In particular, the expansion of electron density at cobalt sites has the $Y_{L=2}^0$ quadrupole ($L = 2$) and even the $Y_{L=1}^0$ dipole ($L = 1$) component lying along the cube diagonals [30].

An electric quadrupole interaction can lead to an effective attractive interaction between electrons at a high symmetry point of the Brillouin zone [43]. The effective interaction between electrons can lower the crystal energy by driving a structural phase transition from $P2_13$ to a phase with lower space symmetry. This implies a breaking of equivalence between four threefold rotational axes. In this case, there is only one relatively high symmetry for the quadrupole ordering: the $R3$ space symmetry ($\Gamma_{\text{th}} C_3^4$, no. 146). In $R3$ symmetry, there is only one threefold rotational axis (e.g., [111] in terms of cubic system) and there are two different channels for the $P2_13 \rightarrow R3$ symmetry lowering [44]. The first involves the quadrupole active mode at the X point [$q_X = \pi/a(1, 0, 0)$] of the Brillouin zone, while the second is connected with the quadrupole mode at the R point [$q_R = \pi/a(1, 1, 1)$]. Which mode actually drives the transformation depends on the energy lowering associated with the mode and requires an additional study. [Both modes (X and R) and the related expansion of the Landau free energy are described in detail in the Appendix.]

As described in the Appendix, the theory shows that the *Lifshitz condition* for both q_X and q_R modes fails, i.e., in the expansion of the Landau free energy in powers of the order parameter components η_i , the antisymmetrical terms, $\eta_k \frac{\partial \eta_i}{\partial x^k} - \eta_i \frac{\partial \eta_k}{\partial x^i}$, etc., are not zero [45]. Consequently, compared to the high-temperature $P2_13$ symmetry that is commensurate, the low-temperature phase is expected to be of the $R3$ symmetry but with an incommensurate wave vector q lying close

to q_X or q_R . That is, both discussed schemes of the $P2_13 \rightarrow R3$ symmetry lowering is a commensurate-incommensurate phase transition induced by quadrupole ordering. Note that one should expect a weak anomaly of the specific heat at the transition because the transformation due to the gradient contribution to the free energy is smoother, which is indeed the case at T_Q in the specific heat measurement [see the inset of Fig. 1(b)]. In this case, the weak anomalous changes of low energy spin/charge dynamics at T_Q , probed by all the ^{59}Co relaxation rates (T_{2L}^{-1} , T_{2G}^{-1} , and T_1^{-1}), may be understood by the coupling between the quadrupole electron density and the spin moment.

The static and dynamical spatial inhomogeneity below $T_0 \sim 30$ K, as inferred from the reduction of the stretching exponent β , the upturn of the resistivity $\rho(T)$, and the additional NMR line broadening, may be understood within the quadrupole ordering scenario, if the incommensurate modulation of the quadrupole electron density exists even above T_Q which could cause a spatial inhomogeneity. It may be worthwhile to recall that an intermediate chiral fluctuating region exists above T_N in MnGe [46], which could be explained by the peculiar band structure.

V. SUMMARY

We have established that the sharp specific heat peak with a negligibly small release of the entropy at $T_Q = 13.7$ K represents a nonmagnetic phase transition, an unprecedented one in the isostructural B20 family of materials. The bulk collective nature of the phase transition at T_Q was verified by probing the clear changes of the ^{59}Co spin-spin and spin-lattice relaxation rates.

The application of group theory suggests that quadrupole electron density arising from the low local site symmetry of the transition metal element in the B20 structure could drive a structural symmetry lowering from $P2_13$ to $R3$. For this symmetry transformation, the Lifshitz condition is violated and therefore the low-temperature $R3$ phase should be incommensurate. Indeed, the commensurate-incommensurate structural phase transition accounts for the tiny sharp peak in the specific heat observed at T_Q . Whereas the (long-range) phase transition takes place at T_Q , the resistivity, the stretching exponent, and the NMR linewidth data point that a static and dynamical spatial inhomogeneity develops at a crossover scale T_0 considerably above T_Q .

It should be emphasized that our group-theoretical arguments could be almost equally applied in the other B20 compounds, and thus the quadrupole-order-driven commensurate-incommensurate phase transition may be ubiquitous in them. However, the tiny anomaly in the specific heat could be easily missed or overwhelmed by other effects, explaining why such a phase transition has hardly been found in these compounds despite many decades of study.

ACKNOWLEDGMENTS

We thank D. A. Salamatin for the analysis of x-ray powder diffractograms. This work was supported by the National Research Foundation of Korea (NRF) grant funded by the Korea government (MSIT) (Grant No. NRF-2020R1A2C1003817). T.K. was supported by the National Science Centre (Poland;

Grant No. UMO-2018/30/M/ST5/00773). Work at Los Alamos National Laboratory was performed under the auspices of the US DOE, Office of Basic Energy Sciences, Division of Material Sciences and Engineering.

APPENDIX A: GROUP-THEORETICAL ANALYSIS

The X point of the B20 Brillouin zone has three rays [at $q_{X,1} = 2\pi/a(1, 0, 0)$, $q_{X,2} = 2\pi/a(0, 1, 0)$, and $q_{X,3} = 2\pi/a(0, 0, 1)$], and the active mode belongs to the two-dimensional irreducible representation E of the little group of X . Therefore, the $P2_13$ space group irreducible representation at the X point (the X_1 irreducible representation) has six components (two components for each ray). A possible mechanism for symmetry lowering from $P2_13$ to $R3$ involves condensation of the component in the form (a, b, a, b, a, b) in the six-dimensional space of X_1 [44]. Thus there are two different order parameter amplitudes: a and b . Condensation of a single component of one ray [for example, at $2\pi/a(1, 0, 0)$] implies that this component changes sign in real space in going from one crystallographic plane (perpendicular to the x axis) to another. Condensation of all three components means that the sign changes in going from one plane to another along the x , y , and z axes. Such structures are called triple- q -antiferroquadrupolar (3- q -AFQ) [43]. In real space the quadrupole electron density is given by

$$\rho(\mathbf{R}_n, \mathbf{r}) = a[\rho_{1x}(\mathbf{r})e^{iq_1\mathbf{R}_n} + \rho_{1y}(\mathbf{r})e^{iq_2\mathbf{R}_n} + \rho_{1z}(\mathbf{r})e^{iq_3\mathbf{R}_n}] + b[\rho_{2x}(\mathbf{r})e^{iq_1\mathbf{R}_n} + \rho_{2y}(\mathbf{r})e^{iq_2\mathbf{R}_n} + \rho_{2z}(\mathbf{r})e^{iq_3\mathbf{R}_n}],$$

where ρ_1 and ρ_2 are active quadrupole functions while \mathbf{R}_n define the n th cubic unit cell of the crystal and \mathbf{r} is the local radius vector, defining the electron density within the n th cubic unit cell.

The rhombohedral (trigonal) quadrupole phase has three basis vectors ($\mathbf{v}_1, \mathbf{v}_2, \mathbf{v}_3$), which in terms of the B20 cubic lattice vectors (e_x, e_y, e_z) are given by [44]

$$\mathbf{v}_1 = 2e_x - 2e_y, \quad \mathbf{v}_2 = 2e_y - 2e_z, \quad \mathbf{v}_3 = 2e_x + 2e_y + 2e_z.$$

The main (hexagonal) axis therefore is along the (1,1,1) main cube diagonal; see Fig. 5(a).

From the condensation scheme one can obtain invariant polynomials, which can be used to construct the Landau expansion of the free energy. Limiting ourselves to the polynomials of the fourth degree in order parameters, we obtain

$$\Phi(P, T, a, b) = \Phi_0 + A(a^2 + b^2) + B_1(a^2 + b^2)^2 + B_2(a^4 + b^4) + B_3a^2b^2 + B^4ab(a^2 - b^2).$$

This expansion can be rewritten in the compact form in terms of the order parameter amplitudes η and ξ :

$$\Phi(P, T, a, b) = \Phi_0 + A\eta^2 + B'_1\eta^4 + B'_2\eta^4 \sin 2\xi \sin 2(\xi + \xi_0).$$

Here $\eta = \pm\sqrt{a^2 + b^2}$ and $\xi = \arccos(a/\eta)$, and B'_1, B'_2 are expressed through B_1, B_2, B_3 , and B_4 . According to the Landau theory of the phase transitions above a certain critical temperature T_Q , which we call the quadrupole transition temperature, we have $A = \alpha(T - T_Q) > 0$, which leads to $\eta = 0$. Below T_Q the parameter A becomes negative, which gives a nontrivial solution $\eta \neq 0, \xi_1 \neq 0$, signaling the appearance

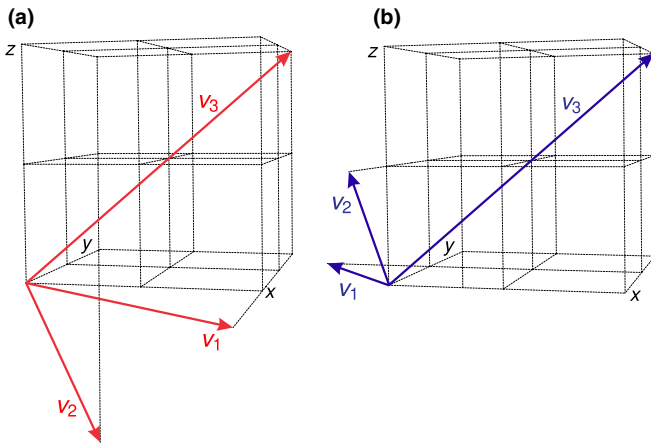


FIG. 5. Rhombohedral (hexagonal) unit cell of $R3$ ($\Gamma_{th} C_3^4$) for the X_1 mode (a) and R_1R_3 mode (b). \mathbf{v}_1 and \mathbf{v}_2 are perpendicular to \mathbf{v}_3 . The angle between \mathbf{v}_1 and \mathbf{v}_2 is $2\pi/3$.

of the quadrupole phase. Notice that, if we find one solution with ξ_1 , we obtain the other solutions with the values $\xi_2 = \xi_1 + \pi/2$, $\xi_3 = \xi_1 + \pi$, and $\xi_4 = \xi_1 + 3\pi/2$. Different values of ξ imply interchange between $\pm a$ and $\pm b$ with different signs (domains of $R3$). In terms of η and ξ_i (here $i = 1$ or $2, 3, 4$) we have

$$a = \eta \cos(\xi_i - \xi_0), \quad b = \eta \sin(\xi_i - \xi_0). \quad (\text{A1})$$

From the expansion of the Landau free energy it follows that the phase transition would be of the second order if the Lifshitz condition [45] had been fulfilled. The Lifshitz condition requires that the coefficient A in the expansion of the free energy as a function of q should have a minimum for $q = q_1$ (and therefore for all other rays of the star, i.e., for $q = q_2$ and $q = q_3$). If the Lifshitz condition is violated, the Landau free energy depends on the quantity

$$\eta \nabla \xi - \xi \nabla \eta \neq 0,$$

and the phase transition leads to the appearance of an incommensurate phase with a long wavelength modulation ($\lambda = 2\pi/k \gg a$) of the order parameter amplitudes η and ξ ,

$$\eta = \eta_0 \cos(\mathbf{k} \cdot \mathbf{R} + \varphi_0), \quad \xi = \xi_0 \sin(\mathbf{k} \cdot \mathbf{R} + \varphi_0), \quad (\text{A2})$$

where $k \ll 1/a$. In this case, the macroscopic modulations of the order parameter amplitudes depend continuously on the thermodynamical parameters, in particular on temperature and pressure. From Eq. (A1) we see that the variation of η causes a gradual change of the quadrupole moments of Co, while the variation of ξ implies a gradual rotation of the quadrupole component. Therefore, Eq. (A2) describes a helical charge density wave, which is presumably directed along the (1,1,1) crystal axis.

The consideration of the R_1R_3 active mode at the R point of the B20 Brillouin zone leads to the same qualitative conclusions. The R point has one ray and the mode belongs to the fourfold irreducible representation R_1R_3 of the $P2_13$ space group. The condensation scheme in the four dimensional space is given by the vector (a, a, a, b) . In real space quadrupole electron density is given by

$$\rho(\mathbf{R}_n, \mathbf{r}) = [a\rho_1(\mathbf{r}) + a\rho_2(\mathbf{r}) + a\rho_3(\mathbf{r}) + b\rho_4(\mathbf{r})]e^{iq_n\mathbf{R}_n},$$

where $\rho_1 - \rho_4$ are four active basis functions. In this case three basis vectors are written as $\mathbf{v}_1 = -e_x + e_y$, $\mathbf{v}_2 = -e_y + e_z$, and $\mathbf{v}_3 = 2e_x + 2e_y + 2e_z$. The unit cell is smaller than for the X_1 mode and the trigonal axis is again along the (1,1,1) direction; see Fig. 5(b).

As before, the Landau free energy expansion in terms of the order parameter amplitude a and b is characteristic of a second order transition (since the Landau free energy for this case is quite complicated, we do not quote it here), but since the Lifshitz condition is violated, the transformation occurs to an incommensurate phase with a long wavelength modulation ($\lambda = 2\pi/k \gg a$) of a and b ,

$$a = a_0 \cos(\mathbf{k} \cdot \mathbf{R} + \varphi_0), \quad b = b_0 \sin(\mathbf{k} \cdot \mathbf{R} + \varphi_0).$$

This relation implies a rotational dependence of the quadrupole density about the vector \mathbf{k} in the Brillouin zone.

-
- [1] D. A. Pshenay-Severin and A. T. Burkov, Electronic structure of B20 (FeSi-type) transition-metal monosilicides, *Materials* **12**, 2710 (2019).
- [2] S. V. Grigoriev, D. Chernyshov, V. A. Dyadkin, V. Dmitriev, E. V. Moskvina, D. Lamago, T. Wolf, D. Menzel, J. Schoenes, S. V. Maleyev, and H. Eckerlebe, Interplay between crystalline chirality and magnetic structure in $\text{Mn}_{1-x}\text{Fe}_x\text{Si}$, *Phys. Rev. B* **81**, 012408 (2010).
- [3] Y. Ishikawa, K. Tajima, D. Bloch, and M. Roth, Helical spin structure in manganese silicide MnSi, *Solid State Commun.* **19**, 525 (1976).
- [4] S. M. Stishov and A. E. Petrova, Itinerant helimagnet MnSi, *Phys.-Usp.* **54**, 1117 (2011).
- [5] B. Lebech, J. Bernhard, and T. Freltoft, Magnetic structures of cubic FeGe studied by small-angle neutron scattering, *J. Phys.: Condens. Matter* **1**, 6105 (1989).
- [6] N. Kanazawa, Y. Onose, T. Arima, D. Okuyama, K. Ohoyama, S. Wakimoto, K. Kakurai, S. Ishiwata, and Y. Tokura, Large Topological Hall Effect in a Short-Period Helimagnet MnGe, *Phys. Rev. Lett.* **106**, 156603 (2011).
- [7] O. L. Makarova, A. V. Tsvyashchenko, G. Andre, F. Porcher, L. N. Fomicheva, N. Rey, and I. Mirebeau, Neutron diffraction study of the chiral magnet MnGe, *Phys. Rev. B* **85**, 205205 (2012).
- [8] N. M. Chitchev, M. V. Magnitskaya, V. A. Sidorov, L. N. Fomicheva, A. E. Petrova, and A. V. Tsvyashchenko, Theoretical and experimental study of high-pressure synthesized B20-type compounds $\text{Mn}_{1-x}(\text{Co}, \text{Rh})_x\text{Ge}$, *Pure Appl. Chem.* **91**, 941 (2019).
- [9] J. Beille, J. Voiron, F. Towfiq, M. Roth, and Z. Y. Zhang, Helimagnetic structure of the $\text{Fe}_x\text{Co}_{1-x}\text{Si}$ alloys, *J. Phys. F: Met. Phys.* **11**, 2153 (1981).
- [10] S. Mulbauer, B. Binz, F. Jonietz, C. Pfleiderer, A. Rosch, A. Neubauer, R. Georgii, and P. Böni, Skyrmion lattice in a chiral magnet, *Science* **323**, 915 (2009).

- [11] T. Nakajima, H. Oike, A. Kikkawa, E. P. Gilbert, N. Booth, K. Kakurai, Y. Taguchi, Y. Tokura, F. Kagawa, and T. hisa Arima, Skyrmion lattice structural transition in MnSi, *Sci. Adv.* **3**, e1602562 (2017).
- [12] W. Münzer, A. Neubauer, T. Adams, S. Mühlbauer, C. Franz, F. Jonietz, R. Georgii, P. Böni, B. Pedersen, M. Schmidt, A. Rosch, and C. Pfleiderer, Skyrmion lattice in the doped semiconductor $\text{Fe}_{1-x}\text{Co}_x\text{Si}$, *Phys. Rev. B* **81**, 041203(R) (2010).
- [13] X. Z. Yu, Y. Onose, N. Kanazawa, J. H. Park, J. H. Han, Y. Matsui, N. Nagaosa, and Y. Tokura, Real-space observation of a two-dimensional skyrmion crystal, *Nature (London)* **465**, 901 (2010).
- [14] Y. Fujishiro, N. Kanazawa, T. Shimojima, A. Nakamura, K. Ishizaka, T. Koretsune, R. Arita, A. Miyake, H. Mitamura, K. Akiba, M. Tokunaga, J. Shiogai, S. Kimura, S. Awaji, A. Tsukazaki, A. Kikkawa, Y. Taguchi, and Y. Tokura, Large magneto-thermopower in MnGe with topological spin texture, *Nat. Commun.* **9**, 408 (2018).
- [15] F. Zheng, F. N. Rybakov, A. B. Borisov, D. Song, S. Wang, Z.-A. Li, H. Du, N. S. Kiselev, J. Caron, A. Kovács, M. Tian, Y. Zhang, S. Blügel, and R. E. Dunin-Borkowski, Experimental observation of chiral magnetic bobbers in B20-type FeGe, *Nat. Nanotechnol.* **13**, 451 (2018).
- [16] C. Pfleiderer, D. Reznik, L. Pintschovius, H. v. Löhneysen, M. Garst, and A. Rosch, Partial order in the non-Fermi-liquid phase of MnSi, *Nature (London)* **427**, 227 (2004).
- [17] R. Ritz, M. Halder, M. Wagner, C. Franz, A. Bauer, and C. Pfleiderer, Formation of a topological non-Fermi liquid in MnSi, *Nature (London)* **497**, 231 (2013).
- [18] A. Barla, H. Wilhelm, M. K. Forthaus, C. Strohm, R. Ruffer, M. Schmidt, K. Koepf, U. K. Rößler, and M. M. Abd-Elmeguid, Pressure-Induced Inhomogeneous Chiral-Spin Ground State in FeGe, *Phys. Rev. Lett.* **114**, 016803 (2015).
- [19] F. Ishii, H. Kotaka, and T. Onishi, Spin-orbit interaction effects in the electronic structure of B20-type CoSi: First-principles density functional study, *JPS Conf. Proc.* **3**, 016019 (2014).
- [20] P. Tang, Q. Zhou, and S.-C. Zhang, Multiple Types of Topological Fermions in Transition Metal Silicides, *Phys. Rev. Lett.* **119**, 206402 (2017).
- [21] D. Takane, Z. Wang, S. Souma, K. Nakayama, T. Nakamura, H. Oinuma, Y. Nakata, H. Iwasawa, C. Cacho, T. Kim, K. Horiba, H. Kumigashira, T. Takahashi, Y. Ando, and T. Sato, Observation of Chiral Fermions with a Large Topological Charge and Associated Fermi-Arc Surface States in CoSi, *Phys. Rev. Lett.* **122**, 076402 (2019).
- [22] Z. Rao, H. Li, T. Zhang, S. Tian, C. Li, B. Fu, C. Tang, L. Wang, Z. Li, W. Fan, J. Li, Y. Huang, Z. Liu, Y. Long, C. Fang, H. Weng, Y. Shi, H. Lei, Y. Sun, T. Qian *et al.*, Observation of unconventional chiral fermions with long Fermi arcs in CoSi, *Nature (London)* **567**, 496 (2019).
- [23] D. S. Sanchez, I. Belopolski, T. A. Cochran, X. Xu, J.-X. Yin, G. Chang, W. Xie, K. Manna, V. Süß, C.-Y. Huang, N. Alidoust, D. Multer, S. S. Zhang, N. Shumiya, X. Wang, G.-Q. Wang, T.-R. Chang, C. Felser, S.-Y. Xu, S. Jia *et al.*, Topological chiral crystals with helicoid-arc quantum states, *Nature (London)* **567**, 500 (2019).
- [24] B. Xu, Z. Fang, M.-Á. Sánchez-Martínez, J. W. F. Venderbos, Z. Ni, T. Qiu, K. Manna, K. Wang, J. Paglione, C. Bernhard, C. Felser, E. J. Mele, A. G. Grushin, A. M. Rappe, and L. Wu, Optical signatures of multifold fermions in the chiral topological semimetal CoSi, *Proc. Natl. Acad. Sci. USA* **117**, 27104 (2020).
- [25] G. Chang, S.-Y. Xu, B. J. Wieder, D. S. Sanchez, S.-M. Huang, I. Belopolski, T.-R. Chang, S. Zhang, A. Bansil, H. Lin, and M. Z. Hasan, Unconventional Chiral Fermions and Large Topological Fermi Arcs in RhSi, *Phys. Rev. Lett.* **119**, 206401 (2017).
- [26] Z. Ni, K. Wang, Y. Zhang, O. Pozo, B. Xu, X. Han, K. Manna, J. Paglione, C. Felser, A. G. Grushin, F. de Juan, E. J. Mele, and L. Wu, Giant topological longitudinal circular photo-galvanic effect in the chiral multifold semimetal CoSi, *Nat. Commun.* **12**, 154 (2021).
- [27] B. Balasubramanian, P. Manchanda, R. Pahari, Z. Chen, W. Zhang, S. R. Valloppilly, X. Li, A. Sarella, L. Yue, A. Ullah, P. Dev, D. A. Muller, R. Skomski, G. C. Hadjipanayis, and D. J. Sellmyer, Chiral Magnetism and High-Temperature Skyrmions in B20-Ordered Co-Si, *Phys. Rev. Lett.* **124**, 057201 (2020).
- [28] J. F. DiTusa, S. B. Zhang, K. Yamaura, Y. Xiong, J. C. Prestigiacomo, B. W. Fulfer, P. W. Adams, M. I. Brickson, D. A. Browne, C. Capan, Z. Fisk, and J. Y. Chan, Magnetic, thermodynamic, and electrical transport properties of the non-centrosymmetric B20 germanides MnGe and CoGe, *Phys. Rev. B* **90**, 144404 (2014).
- [29] F. Carbone, M. Zangrando, A. Brinkman, A. Nicolaou, F. Bondino, E. Magnano, A. A. Nugroho, F. Parmigiani, T. Jarlborg, and D. van der Marel, Electronic structure of MnSi: The role of electron-electron interactions, *Phys. Rev. B* **73**, 085114 (2006).
- [30] C. J. Bradley and A. P. Cracknell, *The Mathematical Theory of Symmetry in Solids* (Clarendon, Oxford, 1972).
- [31] P. Santini, S. Carretta, G. Amoretti, R. Caciuffo, N. Magnani, and G. H. Lander, Multipolar interactions in f-electron systems: The paradigm of actinide dioxides, *Rev. Mod. Phys.* **81**, 807 (2009).
- [32] A. V. Nikolaev and K. H. Michel, Microscopic theory of quadrupole ordering in TmTe, *Phys. Rev. B* **63**, 104105 (2001).
- [33] D. Mannix, Y. Tanaka, D. Carbone, N. Bernhoeft, and S. Kunii, Order Parameter Segregation in $\text{Ce}_{0.7}\text{La}_{0.3}\text{B}_6$: 4f Octopole and 5d Dipole Magnetic Order, *Phys. Rev. Lett.* **95**, 117206 (2005).
- [34] T. Matsumura, S. Nakamura, T. Goto, H. Amitsuka, K. Matsuhira, T. Sakakibara, and T. Suzuki, Low Temperature Properties of the Magnetic Semiconductor TmTe, *J. Phys. Soc. Jpn.* **67**, 612 (1998).
- [35] V. Larchev and S. Popova, The polymorphism of transition metal monogermanides at high pressures and temperatures, *J. Less-Common Met.* **87**, 53 (1982).
- [36] H. Takizawa, T. Sato, T. Endo, and M. Shimada, High-pressure synthesis and electrical and magnetic properties of MnGe and CoGe with the cubic B20 structure, *J. Solid State Chem.* **73**, 40 (1988).
- [37] A. Tsvyashchenko, V. Sidorov, L. Fomicheva, V. Krasnorussky, R. Sadykov, J. Thompson, K. Gofryk, F. Ronning, and V. Ivanov, High pressure synthesis and magnetic properties of cubic B20 MnGe and CoGe, *Solid State Phenom.* **190**, 225 (2012).
- [38] N. Kanazawa, Y. Onose, Y. Shiomi, S. Ishiwata, and Y. Tokura, Band-filling dependence of thermoelectric

- properties in B20-type CoGe, *Appl. Phys. Lett.* **100**, 093902 (2012).
- [39] L. G. Khvostantsev, V. N. Slesarev, and V. V. Brazhkin, Toroid type high-pressure device: history and prospects, *High Press. Res.* **24**, 371 (2004).
- [40] A. V. Tsvyashchenko, High pressure synthesis of RE₆Cu₂₃ compounds (RE = Tb, Dy, Yb, Lu), *J. Less-Common Met.* **99**, L9 (1984).
- [41] G. C. Carter, L. H. Bennett, and D. J. Kahan, *Metallic Shift in NMR* (Pergamon, New York, 1977).
- [42] C. H. Pennington and C. P. Slichter, Theory of Nuclear Spin-Spin Coupling in YBa₂Cu₃O_{7- δ} , *Phys. Rev. Lett.* **66**, 381 (1991).
- [43] A. V. Nikolaev and A. V. Tsvyashchenko, The puzzle of the $\gamma \rightarrow \alpha$ and other phase transitions in cerium, *Phys.-Usp.* **55**, 657 (2012).
- [44] H. T. Stokes and D. M. Hatch, *Isotropy Subgroups of the 230 Crystallographic Space Groups* (World Scientific, Singapore, 1988).
- [45] L. D. Landau and E. M. Lifshitz, *Statistical Physics* (Pergamon Press, Bristol, 1995), Vol. 5.
- [46] M. Deutsch, P. Bonville, A. V. Tsvyashchenko, L. N. Fomicheva, F. Porcher, F. Damay, S. Petit, and I. Mirebeau, Stress-induced magnetic textures and fluctuating chiral phase in MnGe chiral magnet, *Phys. Rev. B* **90**, 144401 (2014).